Detectability of contrast agents for confocal reflectance imaging of skin and microcirculation

Milind Rajadhyaksha
Northeastern University
Center for Subsurface Sensing and Imaging Systems
302 Stearns Center
Boston, Massachusetts 02115
    and
Memorial Sloan-Kettering Cancer Center
Dermatology Service, Department of Medicine
160 East 53rd Street
New York, NY 10022
E-mail: rajadmil@ece.neu.edu

Salvador Gonzalez
Wellman Laboratories of Photomedicine
Massachusetts General Hospital
Harvard Medical School
Bartlett Extension 630
Boston, Massachusetts 02114

James M. Zavislan
University of Rochester
The Institute of Optics
Wilmot Building
Rochester, NY 14627

Abstract. Confocal reflectance microscopy of skin and other tissues *in vivo* is currently limited to imaging at the cellular, nuclear and general architectural levels due to the lack of microstructure-specific contrast. Morphologic and functional imaging at specific organelle and microstructure levels may require the use of exogenous contrast agents in small (nontoxic) concentrations, from which weakly back-scattered light must be detected in real time. We report an analysis based on Mie theory to predict detectability, in terms of signal-to-background and signal-to-noise ratios, of reflectance contrast agents within skin and microcirculation. The analysis was experimentally verified by detectability of (a) intravenously injected polystyrene microspheres that enhance the contrast of dermal microcirculation in Sprague–Dawley rats, and (b) acetic acid-induced compaction of chromatin that enhances nuclear morphology in normal and cancerous human skin. Such analyses and experiments provide a quantitative basis for developing the opto-biochemical properties and use of contrast agents and for designing confocal instrumentation to enable real-time detectability *in vivo.* © *2004 Society of Photo-Optical Instrumentation Engineers.* [DOI: 10.1117/1.1646175]

Keywords: confocal; microscopy; detectability; contrast agents; imaging; skin; microcirculation.

Paper 014016 received Apr. 22, 2003; revised manuscript received Jul. 28, 2003; accepted for publication Jul. 29, 2003.

1 Introduction

The confocal reflectance microscope images nuclear and cellular morphology in the epidermis, microcirculation and collagen in the dermis and other architectural detail in living skin to depths of 200–350 μm, with lateral resolution 0.5–1.0 μm and section thickness (axial resolution) 2–5 μm.[1–5] The optical sectioning with a confocal microscope is comparable to the physical 5 μm sectioning that is typically performed for conventional histology. High-resolution confocal reflectance imaging is based on the detection of singly backscattered light from the optical section. The contrast is due to refractive index variations of organelles and microstructures such as intranuclear chromatin, mitochondria, melanin-containing melanosomes (pigment granules), keratin (protein distribution) and collagen fibrils and bundles.[3–6] The relative contribution of these sources of endogenous contrast to detected signal levels was analyzed by Dunn et al. and others using finite-difference time-domain (FDTD) analysis.[7–11]

Recent research work in light scattering spectroscopy has focused on the characterization of scattered light signals from endogenous sources such as nuclei, organelles and microstructures within cells and tissues, based on Mie theory[12–19] and FDTD analysis[9–11] and goniometric measurements of phase functions, reduced scattering coefficients and other parameters. Hielscher, Mourant, and Bigio et al. have characterized parameters such as size distribution of the scatterers, correlation of large angle scatter to small organelles such as mitochondria and DNA content versus small angle scatter to nuclei,[12–15] and distinguishing normal versus cancerous cells based on small differences in intracellular scatterer (nuclei, organelles) sizes.[16] Saidi, Jacques, and Tittel identified sources of scattering in skin (mainly dermal collagen) based on Mie and Rayleigh modeling.[17] Based on FDTD modeling, Dunn, Drezek and Richards-Kortum et al. provide an understanding of scattering from cells containing heterogenous size and refractive index distribution of organelles.[9–11] Pereleman et al. have demonstrated the ability to determine density and size distribution of epithelial nuclei by extracting the singly scattered component from the multiply scattered diffuse light that is detected.[18,19]

Under real-time, high-resolution confocal reflectance conditions *in vivo*, endogenous sources alone may not provide the high-enough contrast specificity that may be required to distinguish organelles, types of cells, microstructures and other components of tissue. For example, two main sources of contrast in skin are melanin (in pigmented lesions such as melanomas) and keratin (in nonpigmented lesions such as basal cell cancers); often, keratinocytes contain both in complex intermixed spatial distributions. Both melanin and keratin appear bright, grainy and indistinguishable in confocal reflectance images. Thus, exogenous contrast agents may be necessary to enable imaging at organelle- and microstructure-specific levels. Examples of potentially useful contrast agents include liposomes (used for drug delivery), aluminum chloride and aluminum zirconate salts (used in topical skin treat-

ments), intralipid and an evolving class of molecular particles and nano-particles. Detection of exogenous contrast agents *in vivo* with high resolution and in real time will be challenging for two reasons: (a) at a concentration that must be low enough to be nontoxic to tissue, the very small confocal probe volume may not contain sufficient number of contrast agent particles or molecules to produce a strong backscattered signal, and (b) when imaging, the detector may not have long enough integration time to allow each pixel to collect a sufficient number of backscattered photons. Thus, an important factor will be detectability: the detected singly backscattered signal relative to the multiply-scattered background noise (i.e., contrast) and the signal relative to noise (i.e., signal-to-noise ratio) as a function of the optical properties of both the contrast agent and the tissue. A quantitative understanding of detectability will provide the basis for the opto-biochemical design and use of contrast agents as well as optimum design of confocal instrumentation parameters. Gan and Sheppard[20] and Sheppard et al.[21] have presented a detailed analysis of detectability in terms of signal-to-noise ratio, taking into account all sources of noise such as quantum effects, optical instrumentation and object background. In fact, they propose detectability as a rigorous criterion for evaluating confocal microscope performance.[20]

In this paper, we present an analysis based on Mie scattering theory to predict detected (backscattered) signals from and detectability of contrast agents within skin and microcirculation in video-rate confocal reflectance images. The detectability is determined in terms of signal-to-background ratio (image contrast) and signal-to-noise ratio (image quality). The analysis was experimentally verified by imaging and detection of exogenous agents such as polystyrene microspheres in the dermal microcirculation of Sprague–Dawley rats and acetic acid-induced compaction of chromatin within human epidermal nuclei, as well as by measurement of endogenous signals from human epidermis. (For the interested reader: a corresponding analytical model and experimental tests for detectability of fluorescence contrast agents *in vivo* was recently published.[22])

2 Analysis of Detected Signal

In high-resolution confocal reflectance microscopy, the optical section within living skin has been experimentally measured to be 2–5 μm thick when using water immersion objective lenses of numerical apertures (NAs) 0.7–1.2.[4,5] Since the thickness of the optical section is much less than the mean path length ($\sim$20–100 μm) for scattering and absorption in the skin, the imaging is based on the detection of singly backscattered light. The contrast is provided by refractive index variations of organelles and microstructures that are typically of size 0.1–1.0 μm and refractive index 1.34–1.70.

2.1 Mie Theory

Mie's theory is for a homogenous sphere of uniform refractive index (n_1) that is immersed within a homogeneous medium of uniform refractive index (n_2). As such, Mie theory does not apply to living tissues: scattering organelles and microstructures are neither spherical nor homogenous, and the surrounding epidermis or dermis is neither homogenous nor uniform refractive index. Nevertheless, a quantitative under-
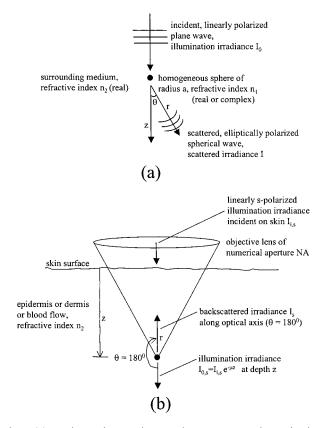

Fig. 1 (a) Conditions for Mie theory: a homogeneous sphere of radius a and refractive index n_1 is within a homogeneous medium of refractive index n_2, and illuminated with linearly polarized plane waves (irradiance I_0), resulting in elliptically polarized spherical scattered waves (irradiance I). When the illumination is linearly *s*- or *p*-polarized, the corresponding scattered irradiance is I_s or I_p as defined in Eqs. (3) and (4); (b) geometry for confocal reflectance imaging: the incident linearly *s*-polarized irradiance on the skin surface is $I_{i,s}$ which decreases exponentially to $I_{0,s}$ when it illuminates a contrast agent at depth *z*. The linearly *s*-polarized backscattered irradiance along the optical axis (at $\theta = 180°$) is given by I_s in Eq. (6).

standing of relative (rather than absolute) detected signals may be obtained by applying Mie theory. Thus, we assume the organelles to be spheres and the surrounding epidermis or dermis to be homogeneous with uniform refractive index; by comparison, exogenous contrast agents such as polystyrene microspheres are, in fact, spherical, homogeneous and of uniform refractive index.

When a linearly polarized plane wave illuminates a homogeneous metallic (absorbing) or dielectric (nonabsorbing) sphere [Fig. 1(a)], the scattered irradiance is[23]

$$I = \frac{F(\theta,\phi)}{k^2 r^2} I_0 \qquad (1)$$

in which

$$F(\theta,\phi) = |S_1(\theta)|^2 \sin^2 \phi + |S_2(\theta)|^2 \cos^2 \phi, \qquad (2)$$

where I_0 is the incident irradiance, r is the radial distance away from the scattering sphere, ϕ is the azimuthal angle and $k = 2\pi/\lambda$ is the wave number ($\lambda = \lambda_0/n_2$). $S_1(\theta)$ and $S_2(\theta)$ define the angular distribution of the complex amplitudes of

the spherically diverging scattered waves that are s- or p-polarized (i.e., perpendicular or parallel with respect to the plane containing the incident and scattered beams), respectively.

The scattered irradiance components that are polarized perpendicular (I_s) or parallel (I_p) with respect to the plane containing the incident and scattered beams are

$$I_s = \frac{|S_1(\theta)|^2}{k^2 r^2} I_{0,s}, \tag{3}$$

$$I_p = \frac{|S_2(\theta)|^2}{k^2 r^2} I_{0,p}, \tag{4}$$

where $I_{0,s}$ and $I_{0,p}$ represent the s- and p-polarized illumination irradiance, respectively. $|S_1(\theta)|^2$ and $|S_2(\theta)|^2$ are functions of three variables n, x, θ where (i) $n = n_1/n_2$ (refractive index of the scattering sphere relative to that of the surrounding medium), (ii) $x = 2\pi a/\lambda$ [circumference of the sphere (of radius a) relative to the illumination wavelength λ in the surrounding medium, where λ is actually λ_0/n_2 for λ_0 being the wavelength in vacuum], and (iii) θ is the angle between the propagation directions of the scattered and incident waves as shown in Fig. 1(a). The functions $|S_1(\theta)|^2$ and $|S_2(\theta)|^2$ have been extensively computed in the form of Legendre polynomials and Bessel functions and their derivatives, and are available in the literature.[24–26] (In this analysis, available computed values of $|S_1(\theta)|^2$ and $|S_2(\theta)|^2$ were used which, as explained in the following section, reasonably represent actual confocal imaging conditions. Further detailed analysis will, of course, require the use of computer code such as from Bohren and Huffman.[27])

2.2 Backscattered Signal in Confocal Images of Skin

In a confocal microscope, the illumination from an objective lens of high NA is a converging spherical wave and we often use circular polarization [Fig. 1(b)], but we assume linearly polarized plane wave illumination. Again, under such approximations, we perform Mie analysis to understand relative (rather than absolute) detected signals from exogenous and endogenous contrast agents within skin. (Further detailed analysis must account for spherical waves and circular polarization as a superposition of two orthogonal linear polarizations.)

Within skin, we expect the illumination irradiance to decrease exponentially with depth (Beer's law), based on experimental measurements of confocally detected signals in excised living skin samples. Therefore, when the nominal linearly s-polarized illumination irradiance on the skin surface is $I_{i,s}$, we expect the irradiance on a scattering particle at a depth z to be

$$I_{0,s} = I_{i,s} e^{-\mu z}, \tag{5}$$

where μ is the extinction coefficient due to scattering and absorption [Fig. 1(b)]. The values for μ reported in the literature vary widely, and hence we chose representative values of 10 mm^{-1} for the epidermis and 25 mm^{-1} for the dermis.[28,29] Thus, $I_{0,s} = 0.60 I_{i,s}$ within the epidermis and $0.29 I_{i,s}$ within the dermis, assuming a depth of 50 μm in either layer. This

depth is typical within human epidermis and for microcirculation in the dermis of Sprague–Dawley rats in which experimental tests were performed.

The detected signal is given by the integration of the backscattered irradiance over the solid angle defined by the NA of the objective lens. For the useful range of water immersion NAs of 0.7–1.2 for imaging skin,[4,5] the solid angles are 0.94–3.57 sr; we commonly use a NA of 0.9 that corresponds to 1.65 sr. Since we are interested in relative detected signals from contrast agents, the detected signal was calculated as the directly backscattered component along the optical axis (i.e., $\theta = 180°$) integrated over 1 sr, using available computed scattered irradiance values.[24–26] (1 sr is a reasonable representation of the above mentioned useful range of solid angles and NAs. Further detailed analysis will, of course, require integration of the detected irradiance over the full NA or full solid angle of the objective lens.)

The illumination wavelength in our near-infrared confocal microscope is 1064 nm, for which $k = 5.9 n_2$ [μm^{-1}]. In the close vicinity (say, $r = 1$ μm) of the scattering particle, Eq. (3) gives the backscattered s-polarized irradiance to be

$$I_s = \frac{|S_1(180°)|^2}{35 n_2^2} I_{0,s} \tag{6}$$

assuming illumination with perpendicular (s) polarization [Fig. 1(b)]. $|S_1(180°)|^2$ represents the backscattered irradiance integrated over 1 sr. [For illumination with parallel (p) polarization, we would use $|S_2(180°)|^2$ to determine the corresponding p-polarized backscattered irradiance. For $n \leq 1.5$, which is typical for both exogenous agents and organelles in the epidermis, both $|S_1(\theta)|^2$ and $|S_2(\theta)|^2$ are constant and approximately equal to each other for $\theta \sim 180° \pm 40°$ (i.e., ~ 1.47 sr)].

The backscattered light decreases exponentially (again, transmission through the epidermis and dermis is 0.60 and 0.29, respectively, for 50 μm depth) before it is remitted, and there is a further 50% loss in transmission through the confocal optics. (The experimentally determined transmission of 50% in the laboratory prototype is low. Higher transmission of up to 80% is possible, as determined in a more recent commercial version that is optimally designed and uses better-quality optics.[4]) Under these conditions, the detected irradiance through the confocal pinhole is

$$I_{\text{det},s} = 5.1 \times 10^{-3} \frac{|S_1(180°)|^2}{n_2^2} I_{i,s}$$

from the epidermis, and $\qquad$ (7)

$$I_{\text{det},s} = 1.2 \times 10^{-3} \frac{|S_1(180°)|^2}{n_2^2} I_{i,s} \quad \text{from the dermis.}$$

$$\tag{8}$$

For optimum sectioning, the pinhole diameter is matched to the illumination spot diameter. At video rate, the detector integration time (pixel time) is 100 ns, and at wavelength of 1064 nm, there are 5.3×10^{18} photons/J. Thus, for video-rate high-resolution near-infrared confocal imaging in skin *in vivo* using objective lens NA of 0.7 (solid angle = 1 sr), the detected signal in photons per pixel is

$$S[\text{photons/pixel}] = 2.7 \times 10^9 \frac{|S_1(180°)|^2}{n_2^2} \times I_{i,s}[\text{Watts}]$$

from the epidermis, and (9)

$$S[\text{photons/pixel}] = 6.4 \times 10^8 \frac{|S_1(180°)|^2}{n_2^2} \times I_{i,s}[\text{Watts}]$$

from the dermis, (10)

where the illumination power ($I_{i,s}$) that is incident on the skin must be defined in Watts.

3 Background Noise

Underlying this detected signal is background noise (B) from the tissue due to the small amount of multiply scattered light from the out-of-focus regions that is collected by the pinhole. Additionally, there may be a small amount of back reflections from the microscope optics. Gan and Sheppard[20] and Sheppard et al.[21] have reported a quantitative model for background noise from both the object and the instrument in their analysis of detectability.

The background noise depends on the site and depth within skin being imaged. In our video-rate confocal microscope, we experimentally measured the maximum background to be 100–500 photons (1–5 nw) when imaging deep in the dermis from where no signals are detected, using 10 mW of illumination power at 1064 nm on the skin.[5] Visually, 100–500 photons produce a faint, diffuse background on the video monitor, observed when imaging at depths exceeding 200–350 μm from where we do not detect any signal.

4 Detectability

A contrast agent is detectable if the backscattered signal (S) is higher than the background (B): detectability is thus quantitatively defined in terms of S/B ratio or contrast.[30–32] The contrast must exceed 1 at minimum and, for practical purposes, be significantly higher. Moreover, when detectable, the image quality and information content from the contrast agent depend on the signal-to-noise (S/N) ratio.[30–32] Our video-rate confocal imaging of skin, oral and other tissues is quantum noise limited, for which the root-mean-square S/N ratio is given by the square root of the number of photoelectrons emitted by the detector photocathode.[5] Quantitatively, the S/N ratio is $\eta S / \sqrt{\eta(S+B)}$ where η is the quantum efficiency of the detector ($\eta = 0.16$ at 1064 nm for the avalanche photodiode in our confocal microscope). The detected signal from a contrast agent will thus be useful if the S/N ratio exceeds 1 at minimum but, in practice, must be much higher.

5 Experimental Detectability of Exogenous Contrast Agents

The detectability predicted by the above analysis was experimentally tested in two applications: (i) using polystyrene microspheres to enhance the brightness and contrast of microcirculation in Sprague–Dawley rats *in vivo* and (ii) acetic acid-induced compaction of chromatin to enhance the brightness and contrast of nuclear morphology in freshly excised skin specimens *ex vivo*. The experiments were performed under a Subcommittee on Research and Animal Care (SRAC)-approved protocol for animal imaging and an Institutional Regulary Board (IRB)-approved protocol for human skin studies at Massachusetts General Hospital.

5.1 Polystyrene Microsphere-Enhanced Microcirculation in Rat Dermis in vivo

The Sprague–Dawley rat is an excellent animal model for testing detectability of contrast agents in microcirculation. The microvasculature consists of very thin μm-sized blood vessels and is well hidden within the dense collagen in the dermis, such that the microcirculation is not visualized in real-time confocal images [Fig. 2(a), control]. The blood flow in the microvessels does not have any contrast relative to the surrounding dermis. When injected intravenously, the polystyrene microspheres enhance the brightness and contrast of the microcirculation, making the blood flow easy to detect and visualize. For polystyrene microspheres of diameters 0.1–1.0 μm and refractive index 1.57 in blood flow at depth of 50 μm, the predicted detected signal is 10^2–10^5 photons/pixel (Table 1). These predicted values are somewhat underestimated since we did not integrate over the full NA of the objective lens or account for the illumination being circularly polarized. Based on the contrast (S/B ratio) in Table 1, we expect to detect polystyrene microspheres of diameter larger than 0.1 μm.

The experiments were carried out on Sprague–Dawley rats (weight 300–400 g, blood volume 70 mL/kg, total blood volume 21–28 mL). The ear was a convenient site to image because we could keep the tissue still during imaging with a mechanical tissue-to-objective lens contact device; details of this device have been reported earlier.[4,5] The device consists of a ring-and-hole template that was attached to the ear of the rat with surgical adhesive (Mastisol, Ferndale Laboratories, MI), such that the same site could be imaged before (control) and after injection of polystyrene microspheres. The rat was anesthetized with an intramuscular injection of ketamine(40–100 mg/kg)/xylazine(4–5 mg/kg), and the contrast agent injected into the femoral vein. Polystyrene microspheres of diameters 0.1, 0.2, 0.5 and 1.0 μm and of refractive index 1.57 in distilled water (Molecular Probes, catalog No. F8888) were injected and tested for contrast enhancement and detectability. Each microsphere size was tested on two rats. Each suspension of microspheres was briefly sonicated, and the injected dosage was adjusted depending on the vendor-specified concentration, such that we expected only a single microsphere in the illuminated confocal probe volume at a time. We used a 60X, 0.9 NA water immersion lens and Nd:yttrium–aluminum–garnet wavelength of 1064 nm, for which the confocal probe volume is estimated to be 9×10^{-12} mL, based on a previously reported analysis.[22] For the range of concentrations of 3.6×10^{10}–5.3×10^{12} microspheres/mL, the dosage was either 1 or 0.1 mL, such that there would be no more than one microsphere in the probe volume. The illumination on the skin was 10 mW. We imaged the dermis and microcirculation before injection (control) and for up to 1 h after. The images were both videotaped in real time as well as captured as single frames with a frame grabber; further instrumentation details are available elsewhere.[4,5] At the end of each experiment, the rat was euthanized with an intra-cardiac injection of pentabarbitol (100 mg/kg).
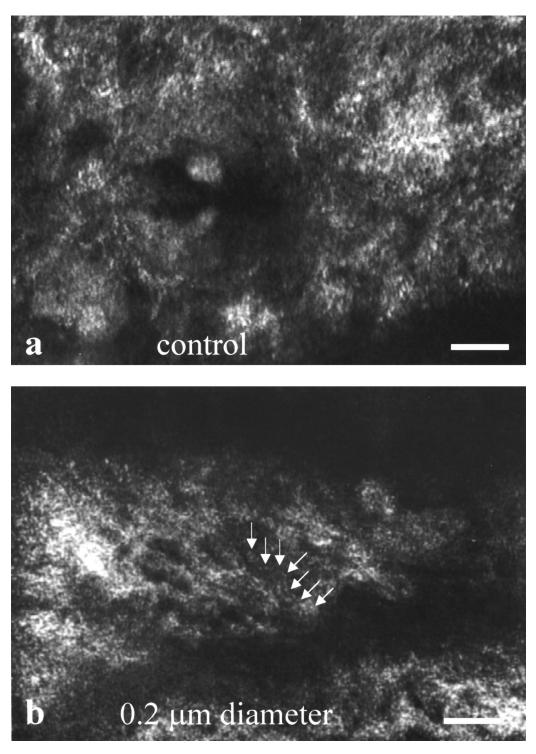
Fig. 2 Confocal reflectance images of Sprague–Dawley rat dermis *in vivo* showing (a) no detectability of microcirculation under normal conditions (control). Blood flow is not detected in the real-time images due to lack of signal and contrast; (b, c, d) detectability of microcirculation (arrows) following intravenous injection of polystyrene microspheres of diameters 0.2, 0.5, and 1.0 μm. The blood flow in microvessels appears as a continuous stream of pixels (arrows) that is easily and convincingly seen in the real-time images but, unfortunately, difficult to fully appreciate in these still images. Objective lens 60X, 0.9 NA water, scale bar 25 μm.

In the dermis of all rats, under normal conditions, we consistently observed the microvasculature to be well hidden within the dense collagen, and the microcirculation was not visualized in real-time confocal images [Fig. 2(a), control]. How-ever, the injection of microspheres of diameter 0.2 μm and larger resulted in the microcirculation being easily and consistently detected at typical measured depths of 50 μm in the dermis [Figs. 2(b), 2(c), and 2(d)]. The blood flow in the
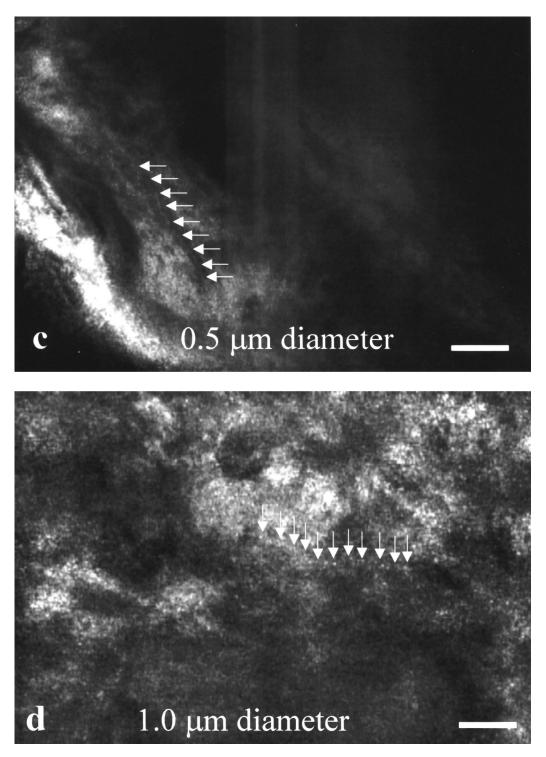
c 0.5 μm diameter

d 1.0 μm diameter

Fig. 2 (*Continued.*)

microvessels is obvious in the real-time images but, unfortunately, not easy to appreciate in these still images. The microcirculation with 0.1-μm-diameter microspheres could not be detected. The microspheres are seen in the images as either one or two pixels, each pixel being equivalent to the lateral resolution ($\sim$0.5 μm) in size. These experimental results confirm the analytical predictions in Table 1.

5.2 Acetic Acid-Enhanced Nuclei in Human Epidermis

The analytical model for detectability provides an understanding for the appearance of nuclei as either dark or bright in confocal reflectance images of living tissues. Nuclei in cervical and skin tissues consistently appear dark, but the topical

Table 1 Predicted detected signals from polystyrene microspheres in blood flow at a depth of 50 μm in the dermis of Sprague–Dawley rats, for incident illumination power ($I_{i,s}$) 10 mW (5.3 $\times 10^9$ photons/pixel) on the skin. The assumed refractive indices are: $n_1 = 1.57$ for the polystyrene microspheres and $n_2 = 1.40-1.33$ for blood at 1064 nm such that $n = 1.12-1.18$. The contrast (S/B ratio) and quality (S/N ratio) are estimated assuming background (B) of 500 photons/pixel and specified quantum efficiency (η) of 0.16 at 1064 nm for the silicon avalanche photodiode in our confocal microscope. The values of S, S/B and S/N are somewhat underestimated due to the approximations in the analysis.

Diameter	a	x	$I_{det,s}$ [nanowatts] (for $n = 1.12-1.18$)	S [photons/pixel] (for $n = 1.12-1.18$)	Contrast (S/B ratio)	Quality (S/N ratio)
0.1 μm	0.05 μm	0.4	0.1–0.8	50–400	0.1–0.8	0.9–5.3
0.5 μm	0.25 μm	2.0	5–20	$2.6 \times 10^3 - 10^4$	5.2–20.0	18.7–39.0
1.0 μm	0.50 μm	4.0	345–640	$1.7 \times 10^5 - 3.1 \times 10^5$	340–620	164.7–222.5

application of 1%–5% acetic acid causes them to appear bright.[6,33,34] This is the well-known aceto-whitening effect that causes a differential brightening of dysplastic tissue relative to normal tissue, and is used for clinical screening of skin, cervical and other epithelial disorders. The brightening of nuclei enhances the contrast and significantly improves detectability of nuclear morphology in basal cell cancers, and is potentially useful for detecting these cancers to guide Mohs micrographic surgery.[6]

The brightening of the nuclei is explained by the Mie analytical prediction of the backscattered detected signal. Under normal conditions, the nucleus contains a diffuse network of thin chromatin filaments that are typically 30–100 nm in diameter and occupy a small volume within.[35,36] We assume the refractive index of the chromatin to be 1.39 on the basis of reported refractive indices for nuclei and intra-nuclear components such as nucleoli, nucleoplasm and chromosomes.[37,38] The surrounding epidermis is of bulk refractive index 1.34.[39] From chromatin filaments of 100 nm size, Eq. (9) predicts the backscattered signal to be 300 photons/pixel from nuclei that are a depth of 50 μm in the epidermis. This signal is within the background ($\sim 100-500$ photons) such that the contrast (S/B ratio) is less than 1 in video-rate images of skin, and thus the nuclei appear dark [Fig. 3(a)]. The acetic acid causes compaction of the chromatin into thick fibers that are 1–5 μm in diameter; the compacted chromatin fills a large fraction of the intra-nuclear volume.[6] From compacted chromatin fibers of 1 μm size, Eq. (9) predicts the backscattered signal to be 4 $\times 10^4$ photons/pixel, and the resulting contrast is 80 and signal-to-noise ratio is 80 (relative to background of 500 photons/pixel). The nuclei thus appear bright [Fig. 3(b)].

Excised thick specimens of human skin were obtained from Mohs surgeries (of basal cell cancers) performed in the Dermatology Surgery Unit at Massachusetts General Hospital. This is skin that remains (and is otherwise discarded) after Mohs surgery; thus, the experiments did not interfere with the routine Mohs surgical procedures and patient care. The skin excisions were rinsed with Dulbecco's phosphate buffered solution (DPBS), washed with 5% acetic acid for 3 min, and then imaged with the confocal microscope. The control images were of skin that was rinsed in DPBS but not washed with acetic acid. We used a 100X, 1.2 NA (measured section thickness 2 μm) for very high-resolution imaging of the ef-

fects of acetic acid on chromatin in a small field of view of 0.15 mm, with illumination at 1064 nm.

In the epidermis, the nuclei normally appear dark in confocal reflectance images [Fig. 3(a)]. After washing the skin specimens with 5% acetic acid for three minutes, the nuclei appear bright [Fig. 3(b)]. We determined the nuclear brightening to be due to the compaction of chromatin, as seen in the high-resolution confocal images and further verified by the
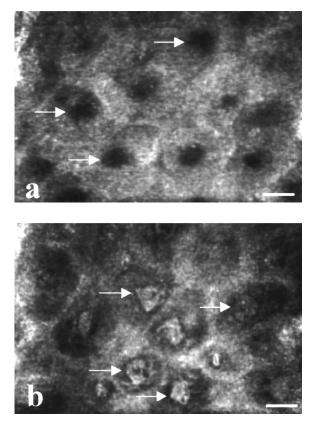

Fig. 3 Confocal reflectance images of human epidermis *ex vivo*, showing (a) nuclei that normally appear dark (arrows); (b) compacted chromatin (arrows) that fills the intra-nuclear volume and makes the nuclei appear bright, after washing with 5% acetic acid. Objective lens 100X, 1.2 NA water, scale bar 10 μm.

Table 2 Predicted detected signals from organelles at a depth of 50 μm in human epidermis, for incident illumination power ($I_{i,s}$) 10 mW (5.3 $\times 10^9$ photons/pixel) on the skin. The assumed refractive indices are: $n_1 = 1.34-1.45$ for the organelles (Refs. 37 and 41–43), 1.40 for mitochondria (Ref. 44) and 1.70 for melanosomes (Ref. 45), and $n_2 = 1.34$ for epidermis (Ref. 39) at 1064 nm such that $n = 1.00-1.08$ for the organelles (for the calculations, we choose $n = 1.05$), 1.05 for the mitochondria and 1.27 for melanosomes. The contrast (S/B ratio) and quality (S/N ratio) are estimated assuming background (B) of 500 photons/pixel and specified quantum efficiency (η) of 0.16 at 1064 nm for the silicon avalanche photodiode in our confocal microscope. The values of S, S/B and S/N are somewhat underestimated due to the approximations in the analysis.

Diameter	a	x	n	$I_{\mathrm{det},s}$	S [photons/pixel]	Contrast (S/B ratio)	Quality (S/N ratio)
Organelles 0.1–1.0 μm	0.05–0.5 μm	0.4–4.0	~1.05	0.03–0.37 nW	$15-2 \times 10^4$	0.03–40.0	0.3–55.9
Mitochondria 1.0 μm	0.5 μm	4.0	1.05	42.7 nW	2.1×10^4	42.0	57.3
Melanosome 0.6–1.2 μm	~0.5 μm	4.0	1.27	4.9 μW	2.4×10^6	4800.0	619.6

corresponding histology. Further details of these experiments and results are available elsewhere.[6]

6 Detectability of Endogenous Contrast Agents

In addition to detectability of exogenous contrast agents, Eqs. (9) and (10) also provide a basis to predict detected signals from endogenous sources of contrast within skin (or any other tissue). The sources of contrast in the epidermis are organelles and microstructures that are typically of 0.1–1.0 μm size[40,41] and refractive index 1.34–1.70.[41–45] For example, mitochondria are of ~1 μm size and refractive index 1.40.[44] The pigment melanin is a major source of contrast in skin,[3] and is present in the form of melanosomes of 0.6–1.2 μm and refractive index 1.70.[45] The bulk refractive index of human epidermis is 1.34, as experimentally determined by optical coherence tomography[39] (as expected, this is close to the refractive index of water, given that the epidermis contains 60%–70% water by volume). The detectability of these organelles, as predicted by Eq. (9), is shown in Table 2. Detected signal levels from the epidermis in an excised specimen of normal skin were measured to be in the range of 10^2-10^4 photons/pixel,[5] when illuminated with 10 mW at 1064 nm. This experimentally observed range is in general agreement with the predicted range in Table 2, taking into consideration that excised (typically, Caucasian types I-III) skin specimens that are obtained from Mohs surgeries tend to be lightly pigmented and with low levels of melanin.

7 Summary and Conclusions

An analysis based on Mie theory provides a quantitative basis to understand the detectability of exogenous and endogenous contrast agents in confocal reflectance images of skin and microcirculation. Although approximate with certain assumptions, the analysis is reasonably accurate in predicting the detectability of exogenous and endogenous contrast agents in the epidermis and in dermal microcirculation *in vivo*. Such analytical predictions and experimental validations of detectability, in terms of detected backscattered signal, contrast (signal-to-background ratio) and quality (signal-to-noise ratio), will be useful in the opto-biochemical design and use of contrast agents as well as the optimization of confocal instrumentation parameters. The use of exogenous contrast agents in humans will require a fundamental analysis of detectability versus toxicity that would lead to instrumentation development and clinical applications. Eventually, an understanding of the detected signals and contrast from microstructural components of tissue may prove useful for potential clinical screening or diagnostic applications.

References

1. K. C. New, W. M. Petroll, A. Boyde, L. Martin, P. Corcuff, J. L. Leveque, M. A. Lemp, H. D. Cavanagh, and J. V. Jester, "In vivo imaging of human teeth and skin using real-time confocal microscopy," *Scanning* **13**, 369–372 (1991).
2. P. Corcuff, G. Gonnord, G. E. Pierard, and J. L. Leveque, "In vivo confocal microscopy of human skin: A new design for cosmetology and dermatology," *Scanning* **18**, 351–355 (1996).
3. M. Rajadhyaksha, M. Grossman, D. Esterowitz, R. H. Webb, and R. R. Anderson, "*In vivo* confocal scanning laser microscopy of human skin: Melanin provides strong contrast," *J. Invest. Dermatol.* **104**, 946–952 (1995).
4. M. Rajadhyaksha, S. G. González, J. M. Zavislan, R. R. Anderson, and R. H. Webb, "*In vivo* confocal scanning laser microscopy of human skin II: Advances in instrumentation and comparison with histology," *J. Invest. Dermatol.* **113**, 293–303 (1999a).
5. M. Rajadhyaksha, R. R. Anderson, and R. H. Webb, "Video-rate confocal scanning laser microscope for imaging human tissues *in vivo*," *Appl. Opt.* **10**, 2105–2115 (1999b).
6. M. Rajadhyaksha, G. Menaker, T. Flotte, P. J. Dwyer, and S. Gonzalez, "Confocal examination of nonmelanoma cancers in thick skin excisions to potentially guide Mohs micrographic surgery," *J. Invest. Dermatol.* **117**, 1137–1143 (2001).
7. A. K. Dunn, C. Smithpeter, A. J. Welch, and R. Richards-Kortum, "Sources of contrast in confocal reflectance imaging," *Appl. Opt.* **35**, 3441–3446 (1996).
8. C. Smithpeter, A. Dunn, R. Drezek, T. Collier, and R. Richards-Kortum, "Near real-time confocal microscopy of cultured amelanotic cells: Sources of signal, contrast agents and limits of contrast," *J. Biomed. Opt.* **3**, 429–436 (1998).
9. A. K. Dunn, C. Smithpeter, A. J. Welch, and R. Richards-Kortum,

"Finite-difference time-domain simulation of light scattering from single cells," *J. Biomed. Opt.* **2**, 262–266 (1997).

10. A. Dunn and R. Richards-Kortum, "Three-dimensional computation of light scattering from cells," *IEEE J. Sel. Top. Quantum Electron.* **2**, 898–905 (1996).

11. R. Drezek, A. Dunn, and R. Richards-Kortum, "Light scattering from cells: Finite-difference time-domain simulations and goniometric measurements," *Appl. Opt.* **38**, 3651–3661 (1999).

12. A. H. Hielscher, J. R. Mourant, and I. Bigio, "Influence of particle size and concentration on the diffuse backscattering of polarized light from tissue phantoms and biological suspensions," *Appl. Opt.* **36**, 125–134 (1997).

13. J. R. Mourant, J. P. Freyer, A. H. Hielscher, A. A. Eick, D. Shen, and T. M. Johnson, "Mechanisms of light scattering from biological cells relevant to noninvasive optical-tissue diagnostics," *Appl. Opt.* **37**, 3586–3593 (1998).

14. J. R. Mourant, M. Canpolat, C. Brocker, O. Esponda-Ramos, T. M. Johnson, A. Matanock, K. Stetter, and J. P. Freyer, "Light scattering from cells: The contribution of the nucleus and the effects of proliferative status," *J. Biomed. Opt.* **5**, 131–137 (2000).

15. J. R. Mourant, T. M. Johnson, S. Carpenter, A. Guerra, T. Aida, and J. P. Freyer, "Polarized angular dependent spectroscopy of epithelial cells and epithelial cell nuclei to determine the size scale of scattering structures," *J. Biomed. Opt.* **7**, 378–387 (2002).

16. J. R. Mourant, A. H. Hielscher, A. A. Eick, T. M. Johnson, and J. P. Freyer, "Evidence of intrinsic differences in the light scattering properties of tumorigenic and nontumorigenic cells," *Cancer Cytopath.* **84**, 366–374 (1998).

17. I. S. Saidi, S. L. Jacques, and F. K. Tittel, "Mie and Rayleigh modeling of visible-light scattering in neonatal skin," *Appl. Opt.* **34**, 7410–7418 (1995).

18. L. T. Perelman, V. Backman, M. Wallace, G. Zonios, R. Manoharan, A. Nusrat, S. Shields, M. Seiler, C. Lima, T. Hamano, I. Itzkan, J. Van Dam, J. M. Crawford, and M. S. Feld, "Observation of periodic fine structure in reflectance from biological tissue: A new technique for measuring nuclear size distribution," *Phys. Rev. Lett.* **80**, 627–630 (1998).

19. V. Backman, R. Gurjar, K. Badizadegan, I. Itzkan, R. R. Dasari, L. T. Perelman, and M. S. Feld, "Polarized light scattering spectroscopy for quantitative measurement of epithelial cellular structures *in situ*," *IEEE J. Sel. Top. Quantum Electron.* **5**, 1019–1025 (1999).

20. X. S. Gan and C. J. R. Sheppard, "Detectability: A new criterion for evaluation of the confocal microscope," *Scanning* **15**, 187–192 (1993).

21. C. J. R. Sheppard, X. Gan, M. Gu, and M. Roy, "Signal-to-noise ratio in confocal microscopes," in *Handbook of Biological Confocal Microscopy*, J. B. Pawley (Ed), Chap. 22, pp. 363–371, Plenum, New York (1995).

22. M. Rajadhyaksha and S. Gonzalez, "Real-time in vivo confocal fluorescence microscopy," *Handbook of Biomedical Fluorescence*, M. A. Mycek and B. Pogue (Eds.), Chap. 5, pp. 143–180, Dekker, New York (2003).

23. H. C. van de Hulst, "Wave propagation in a medium containing scatterers," *Light Scattering by Small Particles*, Chap. 4, pp. 28–39, Dover, New York (1981).

24. W. J. Pangonis, W. Heller, and A. Jacobson, *Tables of Light-Scattering Functions for Spherical Particles*, Wayne State University Press, Detroit (1957).

25. R. O. Gumprecht and C. M. Sliepvich, *Tables of Light-Scattering Functions for Spherical Particles*, The Engineering Research Institute–University of Michigan Press, Ann Arbor (1951).

26. R. H. Boll, J. A. Leacock, G. C. Clark, and S. W. Churchill, *Tables of Light-Scattering Functions*, The Engineering Research Institute–University of Michigan Press, Ann Arbor (1958).

27. C. F. Bohren and D. R. Huffman, *Absorption and Scattering of Light by Small Particles*, Wiley, New York (1983).

28. W. F. Cheong, S. A. Prahl, and A. J. Welch, "A review of the optical properties of biological tissue," *IEEE J. Quantum Electron.* **26**, 2166–2185 (1990).

29. V. V. Tuchin, "Optical properties of tissues with strong (multiple) scattering," *Tissue Optics–Light Scattering Methods and Instruments for Diagnosis*, Chap. 1, pp. 3–108, SPIE Press, Bellingham, WA (2000).

30. D. R. Sandison, R. M. Williams, K. S. Wells, J. Strickler, and W. W. Webb, "Quantitative fluorescence confocal laser scanning microscopy (CLSM)," *Handbook of Biological Confocal Microscopy*, J. B. Pawley (Ed.), Chap. 3, pp. 39–53, Plenum, New York (1995).

31. D. R. Sandison and W. W. Webb, "Background rejection and signal-to-noise optimization in confocal and alternative fluorescence microscopes," *Appl. Opt.* **33**, 603–615 (1994).

32. D. R. Sandison, D. W. Piston, R. M. Williams, and W. W. Webb, "Quantitative comparison of background rejection, signal-to-noise ratio, and resolution in confocal and full-field scanning microscopes," *Appl. Opt.* **34**, 3576–3588 (1995).

33. R. A. Drezek, T. Collier, C. K. Brookner, A. Malpica, R. Lotan, R. R. Richards-Kortum, and M. Follen, "Laser scanning confocal microscopy of cervical tissue before and after application of acetic acid," *Am. J. Obstet. Gynecol.* **182**, 1135–1139 (2000).

34. T. Collier, P. Shen, B. de Pradier, R. Richards-Kortum, A. Malpica, and M. Follen, "Vide confocal microscopy of amelanotic tissue: Dynamics of aceto-whitening enable nuclear segmentation," *Opt. Express* **6**, 40–48 (2000).

35. B. Alberts, D. Bray, J. Lewis, M. Raff, K. Roberts, and J. D. Watson, *Molecular Biology of the Cell*, 2nd ed., pp. 498–499, Garland, New York (1989).

36. D. W. Fawcett, *A Textbook of Histology*, 11th ed., pp. 31–47, Saunders, Philadelphia (1986).

37. A. Brunsting and P. Mullaney, "Differential light scattering from spherical mammalian cells," *Biophys. J.* **14**, 439–453 (1974).

38. J. S. Paul and G. M. Mateyko, "Quantitative interference microscopy of polytene chromosomes," *Exp. Cell Res.* **59**, 227–236 (1970).

39. G. J. Tearney, M. E. Brezinski, J. F. Southern, B. E. Bouma, M. R. Hee, and J. G. Fujimoto, "Determination of the refractive index of highly scattering human tissue by optical coherence tomography," *Opt. Lett.* **20**, 2258–2260 (1995).

40. D. W. Fawcett, *An Atlas of Fine Structure, The Cell: Its Organelles and Inclusions*, Saunders, Philadelphia (1966).

41. L. T. Perelman and V. Backman, "Light scattering spectroscopy of epithelial tissues: Principles and applications," *Handbook of Optical Biomedical Diagnostics*, V. V. Tuchin (Ed.), Chap. 12, pp. 675–724, SPIE, Bellingham, WA (2002).

42. J. Beuthan, O. Minet, J. Helfmann, M. Herrig, and G. Muller, "The spatial variation of the refractive index in biological cells," *Phys. Med. Biol.* **41**, 369–382 (1996).

43. J. S. Maier, S. A. Walker, S. Fantini, M. A. Franceschini, and E. Gratton, "Possible correlation between blood glucose concentration and the reduced scattering coefficient of tissues in the near infrared," *Opt. Lett.* **19**, 2062–2064 (1994).

44. N. N. Boustany, R. Drezek, and N. V. Thakor, "Calcium-induced alterations in mitochondrial morphology quantified in situ with optical scatter imaging," *Biophys. J.* **83**, 1691–1700 (2002).

45. I. A. Vitkin, J. Woolsey, B. C. Wilson, and R. R. Anderson, "Optical and thermal characterization of natural (sepia officinalis) melanin," *Photochem. Photobiol.* **59**, 455–462 (1994).